



Research paper

AIM4RES, an open-source 2.5D finite differences MATLAB library for anisotropic electrical resistivity modeling

Simon Gernez ^{a,*}, Abderrezak Bouchedda ^a, Erwan Gloaguen ^a, Daniel Paradis ^b

^a Institut National de la Recherche Scientifique, Centre Eau-Terre-Environnement, 490 rue de la Couronne, Québec, QC, Canada G1K 9A9

^b Natural Resources Canada, Geological Survey of Canada, 490 rue de la Couronne, Québec, QC, Canada G1K 9A9



ARTICLE INFO

Keywords:

Anisotropy

Finite differences modeling

Electrical resistivity tomography

ABSTRACT

Electrical Resistivity Tomography (ERT) is one of the oldest geophysical techniques, and due to the advances of numerical techniques along with computational resources, it is widely used for geophysical prospecting. It has found various domains of application as it is easy to implement and fast to image the ground resistivity heterogeneity. However, anisotropy, which is another key resistivity parameter, is seldom considered. Although being a well-known phenomenon, its consideration in the characterization process is only recent. Amongst the reasons behind this is the absence of available anisotropic resistivity modeling tools. We present AIM4RES (Anisotropic Inverse Modeling for RESistivity) to that end. This open-source MATLAB library allows for 2.5D forward and inverse anisotropic resistivity modeling based on a finite differences scheme. The inverse problem is solved with a Gauss–Newton algorithm. The regularization coefficient, initial model and constraints can be adjusted from prior knowledge in order to avoid local minima during optimization. Analytical and synthetic studies have been carried out to prove the reliability of AIM4RES. The results demonstrate its ability to identify anisotropy, along with the correct geometry and resistivity amplitude. It is also able to correctly detect isotropy, as the inversion comparison with a previous toolbox already proven working showed. A real case study inversion is carried out to demonstrate that AIM4RES is a relevant tool to use on the field, able to reveal strong anisotropy fields even at short scales.

1. Introduction

Electrical resistivity tomography (ERT) is widely used to image the subsurface at different scales in a non-destructive manner. ERT has been successfully applied to numerous geoscientific domains such as hydrology (Kemna et al., 2002; Hubbard and Rubin, 2005; Ismail et al., 2005), mining and oil exploration (Singh et al., 2004; Bauman, 2005), environmental studies (Chambers et al., 2006; de Franco et al., 2009), geotechnical studies (Santarato et al., 2011), agriculture (Corwin and Lesch, 2003), archeology (Xu and Noel, 1991; Papadopoulos et al., 2010). While electrical resistivity anisotropy of the subsurface is well-known (Maillet, 1947), current modeling practice generally assumes isotropic electrical resistivity fields for 1D (Singh et al., 2005; Ingeman-Nielsen and Baumgartner, 2006) 2D or 3D inversion (Dey and Morrison, 1979; Polydorides and Lionheart, 2002; Binley and Kemna, 2005; Pidlisecky et al., 2006; Pidlisecky and Knight, 2008; Günther and Rücker, 2009; Neyamadpour et al., 2009; Amatyakul et al., 2017) and more recently 4D inversion, repeating the 2D or 3D acquisition at different time steps (Cassiani et al., 2006; LaBrecque and Yang, 2001; Loke et al., 2013; Johnson et al., 2017). However,

preferential deposition modes of the sediments and discrete tectonic constraints on bedrock producing directional fractures may result in an important degree of anisotropy at the investigation scale of an ERT experiment (Al-Hazaimay et al., 2016). For instance, Gernez et al. (2019) observed for sediments in a littoral environment that the ratio of horizontal to vertical resistivity can be up to two orders of magnitude. An erroneous assumption of isotropic conditions may thus result in an incorrect interpretation of the subsurface (Maillet, 1947; Keller and Frischknecht, 1966; Asten, 1974). Anisotropy is therefore a key characterization parameter.

It is only recent that electrical anisotropy is being considered model-wise (Greenhalgh et al., 2010; Herwanger et al., 2004), it is seldom considered for interpretation or in the characterization process (Pain et al., 2003). No available numerical algorithms can handle anisotropic electrical fields to our knowledge, and the existing modeling schemes are usually based on finite elements (Pain et al., 2003; Herwanger et al., 2004; Greenhalgh et al., 2010). We present the development of AIM4RES (Anisotropic Inverse Modeling for RESistivity), a 2.5D forward and

* Corresponding author.

E-mail address: simon.gernez@ete.inrs.ca (S. Gernez).

inverse modeling MATLAB library to infer electrical anisotropy. This library is the first publicly available to use a full numerical finite differences (FD) scheme to estimate anisotropy. AIM4RES is made publicly available on github (<https://github.com/Simoger/AIM4RES>). In this paper, we first briefly present the theory behind electrical anisotropy. Then, we detail our FD implementation, followed by a demonstration of its practical use through synthetic and real cases.

2. Anisotropic electrical conductivity

This section summarizes the theoretical development of electrical anisotropy that is thoroughly detailed by Greenhalgh et al. (2010) and Pain et al. (2003). Anisotropic Electrical Resistivity Tomography (AERT) refers to electric potential measurements generated by a direct current injection with a set of electrodes in an anisotropic domain, and their numerical inversion. Mathematically, electrical anisotropy consists in replacing the scalar electrical conductivity σ (or its reciprocal, electrical resistivity ρ) by a tensor expressing the directional variation of the subsurface electrical conductivity. In 2D, it can be defined in the principal frame $\overline{\sigma}_P$, with the axis defined by the maximum (σ_1) and the minimum (σ_3) conductivity directions, or eigenvectors:

$$\overline{\sigma}_P = \begin{bmatrix} \sigma_1 & 0 \\ 0 & \sigma_3 \end{bmatrix} \text{ with } \sigma_1 \geq \sigma_3 \quad (1)$$

and the geometric frame $\overline{\sigma}_G$, with the axis defined by the horizontal and the vertical:

$$\overline{\sigma}_G = \begin{bmatrix} \sigma_{xx} & \sigma_{xz} \\ \sigma_{xz} & \sigma_{zz} \end{bmatrix} \quad (2)$$

A rotation allows switching from one domain to another:

$$\begin{bmatrix} \sigma_{xx} & \sigma_{xz} \\ \sigma_{xz} & \sigma_{zz} \end{bmatrix} = \begin{bmatrix} \cos \theta & \sin \theta \\ -\sin \theta & \cos \theta \end{bmatrix} \cdot \begin{bmatrix} \sigma_1 & 0 \\ 0 & \sigma_3 \end{bmatrix} \cdot \begin{bmatrix} \cos \theta & -\sin \theta \\ \sin \theta & \cos \theta \end{bmatrix} \quad (3)$$

The angle of anisotropy θ is the angle between the horizontal (σ_H) and the highest (σ_1) conductivity directions. It is then equivalent to use the conductivity in the principal frame or geometrical frame, as we will do in order to take advantage of the benefits of both frames in the calculation and discretization. Note that the isotropic case corresponds to $\sigma_1 = \sigma_3$. The conductivity is also linked to the potential by Ohm's law:

$$\mathbf{J} = \overline{\sigma} \mathbf{E} \quad (4)$$

Where \mathbf{J} is the current density, \mathbf{E} is the electric field and $\overline{\sigma}$ is the conductivity tensor. It leads to the 2.5D forward formulation in the anisotropic case (Zhou et al., 2009):

$$\begin{aligned} -\nabla \cdot \left[\overline{\sigma}(x, z) \cdot \nabla \tilde{\phi}(x, k_y, z) \right] + k_y^2 \sigma_{yy}(x, z) \tilde{\phi}(x, k_y, z) \\ = -\frac{I}{2} \delta(\mathbf{r}(x, z) - \mathbf{r}_s(x_s, z_s)) \end{aligned} \quad (5)$$

where $\tilde{\phi}$ is the potential in the frequency domain, k_y is the wavenumber, $\mathbf{r}(x, z)$ are the coordinates in the computational domain or on its boundaries, I is the current source intensity located at $\mathbf{r}_s(x_s, z_s)$ and δ is the Dirac function. In the 2.5D problem, the missing dimension is taken into account by assuming the 3D nature of the point source current by partially transforming Eq. (5) into the Fourier domain (wavenumber k_y). To that end, σ_{yy} is maintained constant and equal to the higher eigenvalue ($\sigma_{yy} = \sigma_2 = \sigma_1$). In addition, the coefficient of anisotropy λ is used to describe the anisotropy (Maillet, 1947):

$$\lambda = \sqrt{\frac{\sigma_1}{\sigma_3}} \quad (6)$$

3. Finite differences implementation for forward and inverse modeling

In this section, we present the finite differences discretization with surface area modeling algorithm for the forward (Section 3.1) and inverse (Section 3.2) models. Final equations differ from the isotropic case albeit reasoning is similar.

3.1. Forward modeling

This forward modeling section presents the general equations used in the model interior, followed by the boundaries equations.

3.1.1. Model interior

To discretize the Eq. (5), we use a weak finite volumes formulation where the electrical potential is obtained by integrating it over a surface area defined around each potential node (Fig. 1). More precisely, we extend the finite differences area discretization formulation of Dey and Morrison (1979) to the anisotropic case. The model is composed of n_c horizontal nodes and n_r vertical nodes. The conductivity tensor $\sigma_{i,j}$ is defined in the whole white cell of area $\Delta x_i * \Delta z_j$. The potential $\tilde{\phi}_{i,j}$ is defined in the whole gray cell of area $\Delta A_i, j = 1/2\Delta x_{i-1} * 1/2\Delta x_i * 1/2\Delta z_{j-1} * 1/2\Delta z_j$ and contour L . We solve the problem integrating Eq. (5) over the surface:

$$-\iint_{\Delta A_{i,j}} \left[\nabla \cdot (\overline{\sigma} \cdot \nabla \tilde{\phi}) + k_y^2 \sigma_{yy} \tilde{\phi} \right] dx dz = \iint_{\Delta A_{i,j}} \frac{I}{2} \delta(\mathbf{r}) dx dz \quad (7)$$

Eq. (6) stands for any position inside the model space $\Omega = \{(x_i, y_j) | i = 2, \dots, n-1; j = 2, \dots, m-1\}$. We integrate it over the shaded area $\Delta A_{i,j}$ presented on the Fig. 1. Using the two-dimensional divergence theorem, the first term of Eq. (7) becomes:

$$-\iint_{\Delta A_{i,j}} \nabla \cdot (\overline{\sigma} \cdot \nabla \tilde{\phi}) dx dz = -\oint_L (\overline{\sigma} \cdot \nabla \tilde{\phi}) \cdot \mathbf{n} dl \quad (8)$$

With \mathbf{n} the outer normal at each point on the contour L . In particular, the anisotropic form of the previous dot product is:

$$\overline{\sigma} \cdot \nabla \tilde{\phi} = \begin{bmatrix} \sigma_{xx} \frac{\partial \tilde{\phi}}{\partial x} + \sigma_{xz} \frac{\partial \tilde{\phi}}{\partial z} \\ \sigma_{xz} \frac{\partial \tilde{\phi}}{\partial x} + \sigma_{zz} \frac{\partial \tilde{\phi}}{\partial z} \end{bmatrix} \quad (9)$$

This contour integral is calculated over segments 1 to 8 (Fig. 1). We detail here the discretization on segment 1:

$$\mathbf{n} = \begin{bmatrix} 0 \\ -1 \end{bmatrix}$$

$$(\overline{\sigma} \cdot \nabla \tilde{\phi}) \cdot \mathbf{n} = -\sigma_{xz} \frac{\partial \tilde{\phi}}{\partial x} - \sigma_{zz} \frac{\partial \tilde{\phi}}{\partial z} \quad (10)$$

The derivative of $\tilde{\phi}$ with respect to z is calculated using a first-order difference scheme:

$$\frac{\partial \tilde{\phi}}{\partial z} = \frac{\tilde{\phi}_{i,j} - \tilde{\phi}_{i,j-1}}{\Delta z_{j-1}} \quad (11)$$

As the first-order difference approximation of the derivative of $\tilde{\phi}$ with respect to x at segment 1 position is not defined, we used the second-order difference scheme (van Es et al., 2014):

$$\frac{\partial \tilde{\phi}}{\partial x} = \frac{\tilde{\phi}_{i+1,j} - \tilde{\phi}_{i-1,j} + \tilde{\phi}_{i+1,j-1} - \tilde{\phi}_{i-1,j-1}}{2(\Delta x_{i-1} + \Delta x_i)} \quad (12)$$

Eq. (10) integration along the edge segment 1 results in:

$$\begin{aligned} -\int_{L_1} (\overline{\sigma} \cdot \nabla \tilde{\phi}) \cdot \mathbf{n} dl = \\ \left[\sigma_{xz} \frac{\phi_{i+1,j} - \phi_{i-1,j} + \phi_{i+1,j-1} - \phi_{i-1,j-1}}{2(\Delta x_{i-1} + \Delta x_i)} + \sigma_{zz} \frac{\phi_{i,j} - \phi_{i,j-1}}{\Delta z_{j-1}} \right] \frac{\Delta x_i}{2} \end{aligned} \quad (13)$$

Integrating Eq. (7) along all the segments forming contour L (Eq. (8) and Fig. 1), the following general finite differences equation is obtained:

$$\begin{aligned} C_{ij}^P \cdot \tilde{\phi}_{i,j} + C_{ij}^L \cdot \tilde{\phi}_{i-1,j} + C_{ij}^R \cdot \tilde{\phi}_{i+1,j} + C_{ij}^T \cdot \tilde{\phi}_{i,j-1} \\ + C_{ij}^B \cdot \tilde{\phi}_{i,j+1} + C_{ij}^{TL} \cdot \tilde{\phi}_{i-1,j-1} \\ + C_{ij}^{BL} \cdot \tilde{\phi}_{i-1,j+1} + C_{ij}^{TR} \cdot \tilde{\phi}_{i+1,j-1} + C_{ij}^{BR} \cdot \tilde{\phi}_{i+1,j+1} = \frac{I}{2} \delta(x_s) \delta(z_s) \end{aligned} \quad (14)$$

or under its matrix equivalent formulation:

$$C \tilde{\phi} = S \quad (15)$$

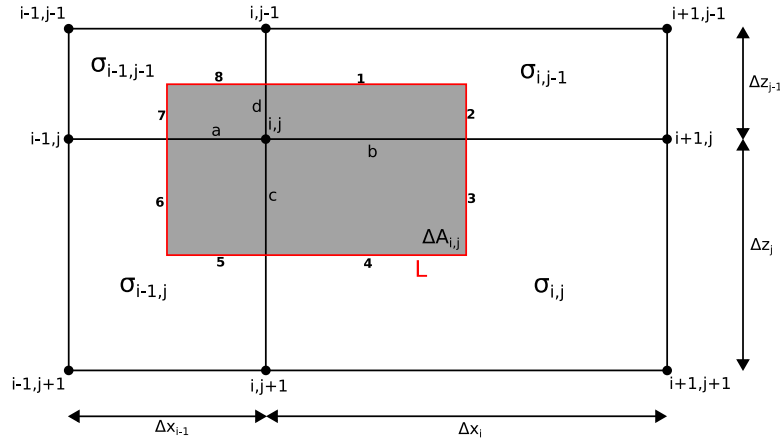


Fig. 1. Regular grid. Regular grid used for the computational discretization. The conductivity $\bar{\sigma}$ is defined inside the white cells (4 conductivity values are displayed: $\sigma_{i,j}$, $\sigma_{i-1,j}$, $\sigma_{i,j-1}$, $\sigma_{i-1,j-1}$), the potential $\tilde{\phi}_{i,j}$ is defined in the gray cell of area $\Delta A_{i,j}$ delimited by the contour L (in red), cut into eight segments numbered from 1 to 8. Segments a to d are used in the boundary calculus.

where C is the capacitance matrix composed of the coupling coefficients C^X , $\tilde{\phi}$ is the unknown potentials vector at grid nodes and S is the source vector containing $I/2$ at the current electrode positions. The full finite differences formulations of Eqs. (7) and (14) are given in Appendix A in order to preserve the readability of the paper. As the formulation of C is generally not symmetric, the solution of Eq. (15) is obtained by LU decomposition. Nevertheless, remarkable anisotropy distributions, like vertically transverse isotropy (VTI), cancel the cross component σ_{xz} of the conductivity tensor, making C symmetric and allowing the use of Cholesky decomposition, faster than LU decomposition.

3.1.2. Model boundaries

The surface nodes ($i = 2, \dots, n-1$; $j = 1$) are considered as a free surface. A Neumann condition is imposed on this edge, represented by the segments a and b in Fig. 1:

$$\sigma_{i,1} \frac{\partial \tilde{\phi}_{i,1}}{\partial n} = 0 \quad i = 2, \dots, n-1 \quad (16)$$

The left and right limits (segments c and d in Fig. 1) and bottom limits (segments a and b in Fig. 1) are controlled by a mixed boundary condition on the nodes $\{(x_i, y_j) \mid i = 1, \dots, n \text{ and } j = 1; i = 1, \dots, n \text{ and } j = m; i = 1 \text{ and } j = 1, \dots, m; i = n \text{ and } j = 1, \dots, m\}$ as proposed by Zhou et al. (2009):

$$(\bar{\sigma} \cdot \nabla \tilde{\phi}) \cdot \mathbf{n} + v \tilde{\phi} = 0 \quad (17)$$

where

$$v = \frac{k_y}{2\sqrt{a}} \cdot \frac{K_1(k_y\sqrt{a})}{K_0(k_y\sqrt{a})} (\bar{\sigma} \cdot \nabla a) \cdot \mathbf{n} \quad (18)$$

with

$$a = \frac{1}{\rho_{yy}} (x^2 \rho_{xx} + 2xz \rho_{xz} + z^2 \rho_{zz}) = \frac{1}{\rho_{yy}} \cdot [x \ z] \begin{bmatrix} \rho_{xx} & \rho_{xz} \\ \rho_{xz} & \rho_{zz} \end{bmatrix} \begin{bmatrix} x \\ z \end{bmatrix} \quad (19)$$

3.2. Inverse modeling

The AERT inverse problem is ill-posed, nonlinear and generally underdetermined. Also, the number of parameters to be determined is two or three times ($\sigma_1, \sigma_3, \theta$) greater than for ERT inverse problem. In our implementation, inversion is solved using Tikhonov regularization method (Tikhonov and Arsenin, 1977). It involves the minimization of a functional that is the sum of a nonlinear data misfit term and a regularization term. The latter prevents the overfit of unwanted features like the noise and support the a priori on the spatial distribution of the parameters (LaBrecque et al., 1996):

$$O(m) = \|F(\Sigma) - \tilde{\phi}\|_2^2 + \gamma \|W_c C \cdot \Sigma\|_2^2 \quad (20)$$

Where F is the forward problem operator, $\tilde{\phi}$ is the vector of measured potentials, C is the regularization matrix, Σ is the parameters vector ($\Sigma = [\sigma_1, \sigma_3, \theta]$), W_c is the weighting parameters matrix and γ is the regularization parameter. The first term of Eq. (20) represents the misfit between the observed data and the computed data. The second term is the regularization term. The regularization matrix has the following form:

$$C = \alpha_x D_x + \alpha_z D_z + \alpha_s I \quad (21)$$

where I is the identity matrix and D_x and D_z are the first or second derivative matrices in the x and z directions respectively, smoothed by the α coefficients. As ERT is a nonlinear problem, the solution is iteratively computed by approximating F with a first-order Taylor expansion (Tikhonov and Arsenin, 1977; Menke, 1989). Eq. (20) thus becomes:

$$O(m) = \|J \Delta \Sigma - \tilde{\phi}\|_2^2 + \gamma \|W_c C \cdot \Sigma\|_2^2 \quad (22)$$

where $\Delta \Sigma$ is the model variation and J the sensitivity matrix. The problem is iteratively solved using a Gauss–Newton algorithm. The sensitivity matrix is calculated using the adjoint equation approach as proposed by Greenhalgh et al. (2009). For the 2.5D case, the sensitivity expression is given by:

$$\frac{\partial \tilde{\phi}}{\partial p} = -2 \left\{ \frac{\partial \sigma_{xx}}{\partial p} \frac{\partial \tilde{\phi}}{\partial x} \frac{\partial G}{\partial x} + \frac{\partial \sigma_{zz}}{\partial p} \frac{\partial \tilde{\phi}}{\partial z} \frac{\partial G}{\partial z} + \frac{\partial \sigma_{xz}}{\partial p} \left(\frac{\partial \tilde{\phi}}{\partial x} \frac{\partial G}{\partial z} + \frac{\partial \tilde{\phi}}{\partial z} \frac{\partial G}{\partial x} \right) + k_{yy}^2 \frac{\partial \sigma_{yy}}{\partial p} \tilde{\phi} G \right\} \quad (23)$$

where $\tilde{\phi}$ and G are respectively the potential and the Green's function, and p assumes any of the values $\sigma_1, \sigma_3, \theta$. Its explicit finite differences development is given in Appendix B. To speed up the convergence and to avoid any bad conditioning of the capacitance matrix, logarithmic values of conductivity are considered (Bouchedda, 2010). It also ensures positive values for the inverted conductivity parameters. In vertically transverse isotropic (VTI) medium, the angle of anisotropy is zero. In this case, the anisotropic inversion problem can be carried out using only the first two parameters σ_1 and σ_3 . AERT inversion efficiency relies upon the sensitivity of the used array configurations. A weighting matrix W_c is implemented to penalize the oversensitive regions in the model. Two formulations (distance-based and sensitivity-based) have been implemented for W_c (both from Li and Oldenburg (1996)). By default, the initial model Σ is an anisotropic homogeneous model, and can be replaced by a user defined initial model. Finally, we have also implemented a constrained inverse modeling using well log resistivities. Note that our algorithm allows to choose to invert only the

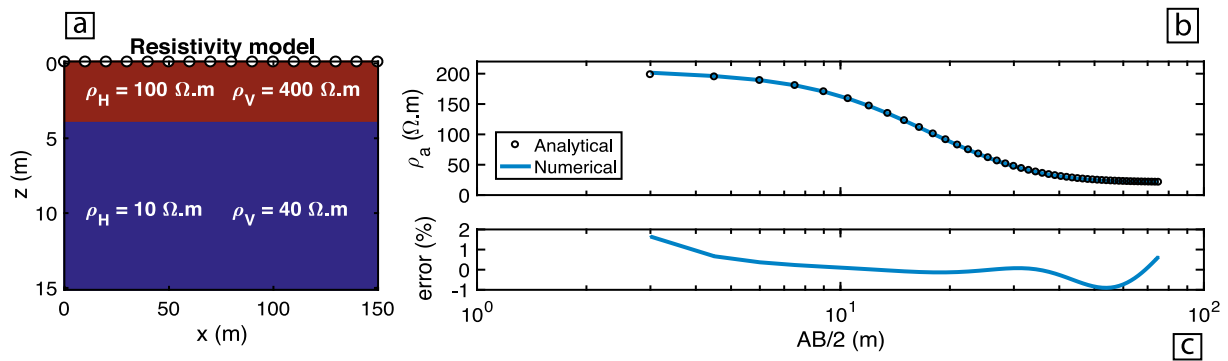


Fig. 2. Forward modeling validation, model 1. [a] Synthetic resistivity model. White dots represent the electrode locations at the surface. [b] Analytical and numerical values of apparent resistivity (ρ_a) from a surface Wenner sounding and [c] their relative error.

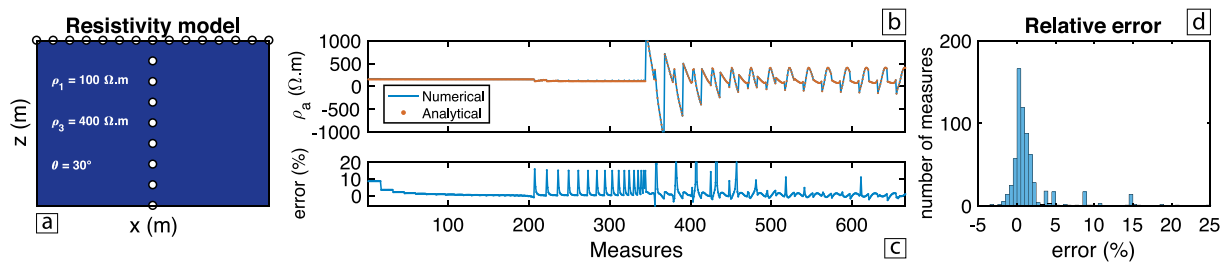


Fig. 3. Forward modeling validation, model 2. [a] Synthetic resistivity model. White dots represent the electrode locations at the surface and in depth. [b] Analytical and numerical values of apparent resistivity (ρ_a) and [c] their relative error. Combination of arrays used: measures 1 to 206 correspond to a Wenner array, measures 207 to 344 correspond to borehole quadrupoles and measures 345 to 666 correspond to surface-borehole quadrupoles. [d] Histogram of the relative error ([c]). 92% of the error values are lower than 5%.

two conductivity parameters in the case of a vertical transverse isotropy (VTI), forcing the angle of anisotropy to be zero. When this assumption can be made, based on complementary knowledge of the subsurface (e.g., geology), the underdetermination of the problem is lowered and the problem is better solved.

4. Forward and inverse model validation

4.1. Forward modeling

To verify the accuracy of our forward modeling code, the numerical response was compared to the analytic response from two synthetic models. In the first experiment, a two-layer anisotropic VTI resistivity model is considered. The horizontal and vertical resistivities are 100 Ω m and 400 Ω m respectively for the first layer, and 10 Ω m and 40 Ω m respectively for the second layer. The angle of anisotropy is null in the whole space. 1D vertical electrical sounding data were simulated using Wenner array by varying $AB/2$ from 3 m to 150 m. The model is discretized using a 0.25 m \times 0.25 m squared cells grid. The results are compared to the analytic solution from Telford et al. (1990). The comparison between numerical and analytical solutions shows an error below 2% (Fig. 2). In the second experiment, we consider a homogeneous anisotropic model with an angle of anisotropy $\theta = 30^\circ$. Resistivity values are $\rho_1 = 100 \Omega$ m and $\rho_3 = 400 \Omega$ m. A combination of multiple arrays (206 data from surface Wenner; 138 data from borehole quadrupoles and 322 data from surface-borehole quadrupoles) is used. The comparison between numerical and analytical (Li and Uren, 1998) solutions shows a low error (92% of the error is lower than 5%, Fig. 3). These two models demonstrate the capacity of our numerical modeling tool to handle anisotropic electrical flow. The difference between analytical and numerical solutions is very low as shown by the error measurement. Further analysis of the error shows that the highest error values on Fig. 3 correspond to apparent resistivities associated with large geometric factors with potential measures very close to zero. A smaller grid step improves the error at the cost of an increased

computational time, and a compromise between admissible precision and time cost has to be found. Another way to reduce the error is to use adapted quadrupole configurations presenting smaller geometric factors when possible.

4.2. Inverse modeling

4.2.1. Anisotropic case

We use the same model as in Fig. 2 to validate our inverse modeling test. The horizontal and vertical resistivities are $\rho_H = 100 \Omega$ m and $\rho_V = 400 \Omega$ m respectively for the first layer, and $\rho_H = 10 \Omega$ m and $\rho_V = 40 \Omega$ m respectively for the second layer. $\lambda = 2$ in the whole section. 50 one meter spaced electrodes are used at the surface and 15 one meter spaced electrodes are used in the borehole. The protocol used is made of:

- 1 surface Wenner array (392 quadrupoles),
- 1 in-hole dipole-dipole array (138 quadrupoles),
- 1 surface-borehole array (322 quadrupoles).

The synthetic potentials are inverted using the following numerical parameters:

- $\gamma = 1$,
- $\lambda_i = 2$ (anisotropy of the initial model),
- $\rho_i^{xx} = M$ and $\rho_i^{zz} = \lambda_i * \rho_i^{xx}$. The initial model is homogeneous, where M is the apparent resistivity median.

The results of the inversion are shown in Fig. 4. The length and the depth of the model are 50 m and 15 m, respectively. However, the presented inverted model is cropped to be displayed between $x = 15$ m and $x = 35$ m, and $z = 0$ m and $z = 15$ m. The sensitivity of the protocol is weak outside this area and therefore the inverted model poorly resolved. Let us notice that from $z = 10$ m and deeper, the sensitivity of the protocol used drop due to the lack of measurement. The inverted model reproduces the layer well with a correct thickness and a consistent resistivity amplitude. Anisotropy is homogeneously

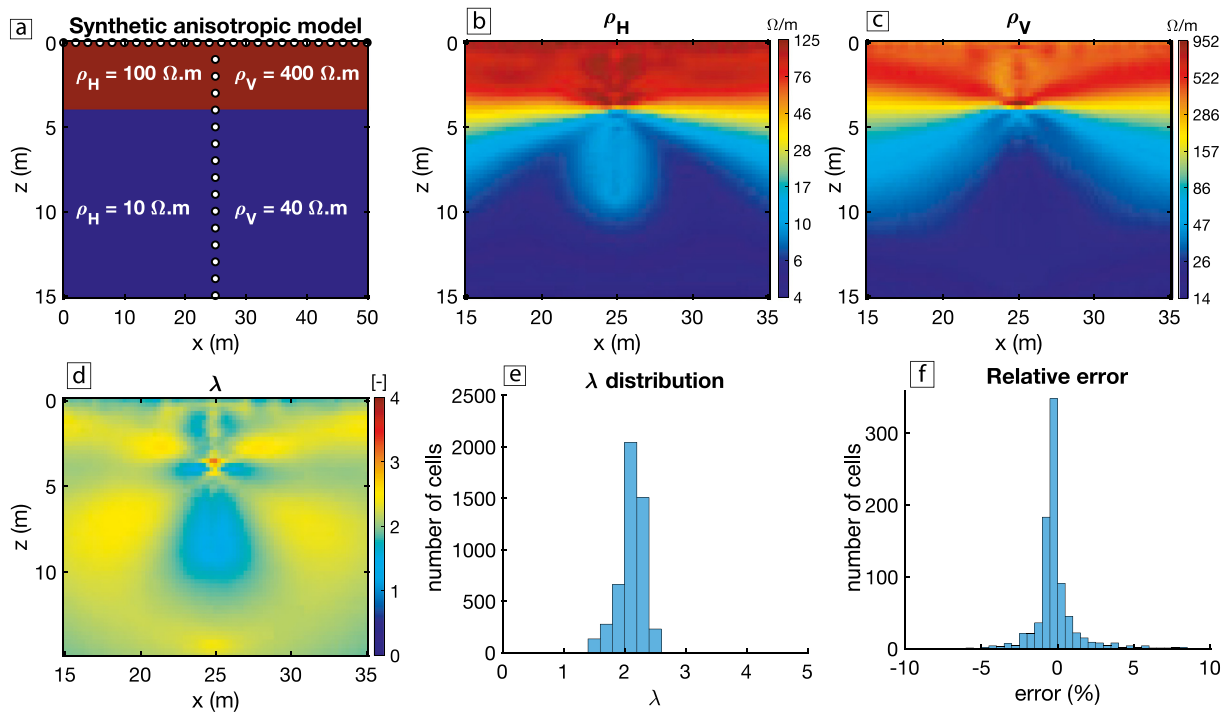


Fig. 4. Synthetic anisotropic study. [a] Anisotropic resistivity model. The white dots represent the electrode locations. [b, c, d] are respectively the horizontal resistivity component ρ_H , the vertical resistivity component ρ_V and the anisotropy λ sections displayed between $x = 15$ m and $x = 35$ m, and between $z = 0$ m and $z = 15$ m. Note the logarithmic color scale. [e] Anisotropy distribution. [f] Relative error between the true synthetic and computed apparent resistivities.

equal to 2 in the whole section (Fig. 4.d), and well defined in the inverted anisotropy section as shown in Figs. 4.b and 4.c. The histogram Fig. 4.e shows anisotropy values closely distributed around 2, which is the true anisotropy value. The final relative error is obtained comparing the true apparent resistivity to the apparent resistivity computed from the inverted model (Fig. 4.f). It shows a small error between the true and computed apparent resistivities, confirming the validity of the inverted model.

4.2.2. Isotropic case

The anisotropic inversion of an isotropic model is also calculated to demonstrate the algorithm ability to correctly adjust any degree of anisotropy of the subsurface. The isotropic synthetic model is composed of a 4 m thick layer over a semi-infinite space. The horizontal and vertical resistivities are $\rho_H = 200 \Omega \cdot m$ and $\rho_V = 200 \Omega \cdot m$ respectively for the first layer, and $\rho_H = 20 \Omega \cdot m$ and $\rho_V = 20 \Omega \cdot m$ respectively for the second layer. $\lambda = 1$ in the whole section. 50 one meter spaced electrodes are used at the surface and 15 one meter spaced electrodes are used in the borehole. The protocol used is made of:

- 1 surface Wenner array (184 quadrupoles),
- 1 in-hole dipole-dipole array (72 quadrupoles),
- 1 surface-borehole array (326 quadrupoles).

Fig. 5 shows the results of the inversion of the synthetic potentials using the following numerical parameters: $\gamma = 1$, $\lambda_i = 1$ and $\rho_i^{xx} = \rho_i^{zz} = M$ with M being the apparent resistivity median obtained with the forward model. Figs. 5.b and 5.c show that isotropy is well defined in the cropped section, despite the apparition of a weak artifact in the deepest section of the ρ_H section (Fig. 5.b). This artifact is due to the lack of sensitivity of the array used. Nevertheless, Fig. 5.e shows that anisotropy is closely distributed around the value $\lambda = 1$. In Figs. 5.b and 5.c, the layer is well defined with the correct thickness, and consistent resistivity values on both the horizontal and vertical components. Finally, Fig. 5.f shows the relative error between the true original apparent resistivities and the apparent resistivities computed

on the inverted model. As much as 8% of the measures have an error lower than 10%, and 67% of the measures have an error lower than 5%. The inverted model corresponds to the true synthetic model, and the apparent resistivities comparison both show the ability of our algorithm to produce good quality inverted models.

The inverted isotropic model with the anisotropic algorithm is also compared to ERT2D, the original isotropic algorithm upon which the anisotropic algorithm was built on (Boucheddou, 2010). The same apparent resistivities from the anisotropic forward modeling are used (the model resistivities still are $\rho = 200 \Omega \cdot m$ for the first layer and $\rho = 20 \Omega \cdot m$ for the second layer). Fig. 6.b shows a consistent inverted model, with very weak artifacts. The computed apparent resistivities from the inverted model are very close to the true apparent resistivities Fig. 6.c. Both isotropic and anisotropic modeling lead to a good characterization of the subsurface resistivity, with correct layer thickness and consistent resistivity amplitudes. The isotropic inverse modeling shows a smaller error and artifacts less marked than the model resulting from the anisotropic inverse modeling. The residual analysis from Fig. 6.f shows that the highest errors come from the deepest surface-borehole measurements. The deepest part of the model is the least well solved as it is characterized by the fewest measurements. The error is also increased by two additional effects. First, the underdetermination is higher for the anisotropic problem, resulting in a greater variability in the least sensitive areas, and the bottom of the model is less sensitive. Then, the protocol measurements are not equally sensitive to the different components of the resistivity tensor. Surface measurements are sensitive to both ρ_H and ρ_V , the in-hole measurements are more sensitive to ρ_H , and the surface-borehole measurements are variably sensitive to both ρ_H and ρ_V according to their geometry. These variable sensitivities increase the inconsistencies between the horizontal and vertical resistivity sections where they differ the most, increasing the error associated with the measurements performed in these areas. Nevertheless, anisotropic inverse modeling errors are low and inverted model consistent with the synthetic true model, demonstrating the ability of our algorithm to solve both isotropic and anisotropic problems.

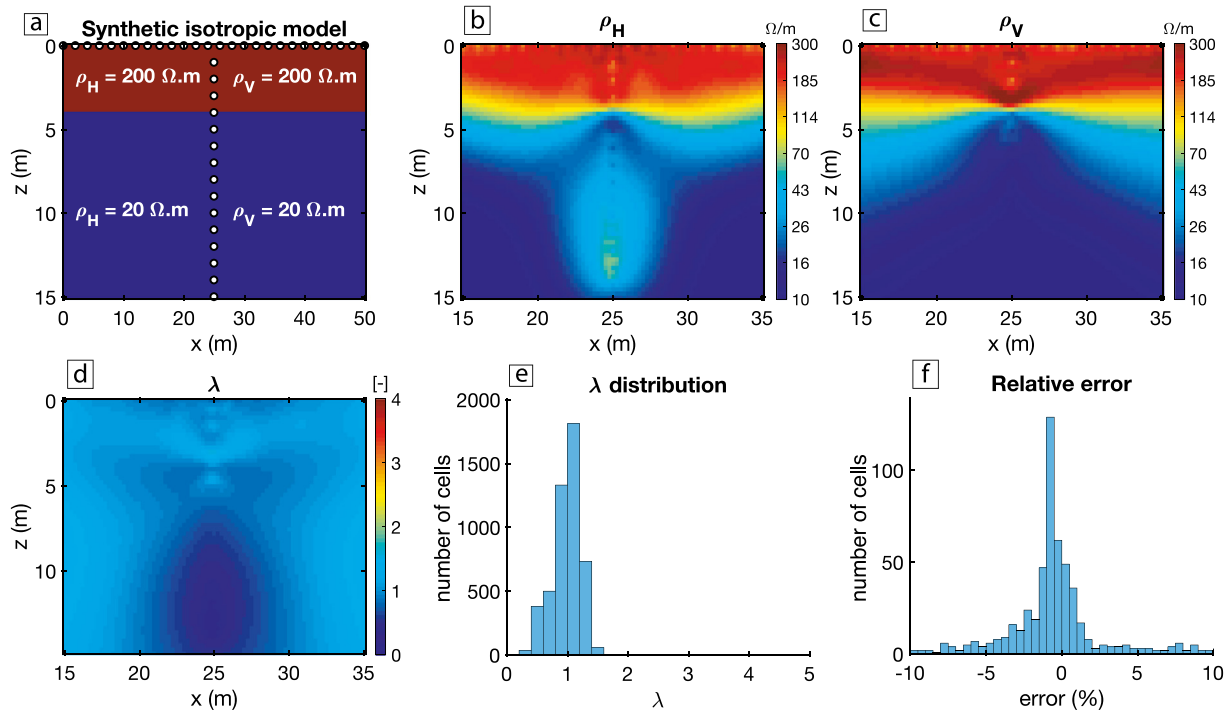


Fig. 5. Synthetic isotropic study. [a] Isotropic resistivity model. The white dots represent the electrode locations. [b, c, d] Respectively the horizontal resistivity component ρ_H , the vertical resistivity component ρ_V and the anisotropy λ sections displayed between $x = 15$ m and $x = 35$ m, and between $z = 0$ m and $z = 15$ m. Note the logarithmic color scale. [e] Anisotropy distribution. [f] Relative error between true synthetic and computed apparent resistivities.

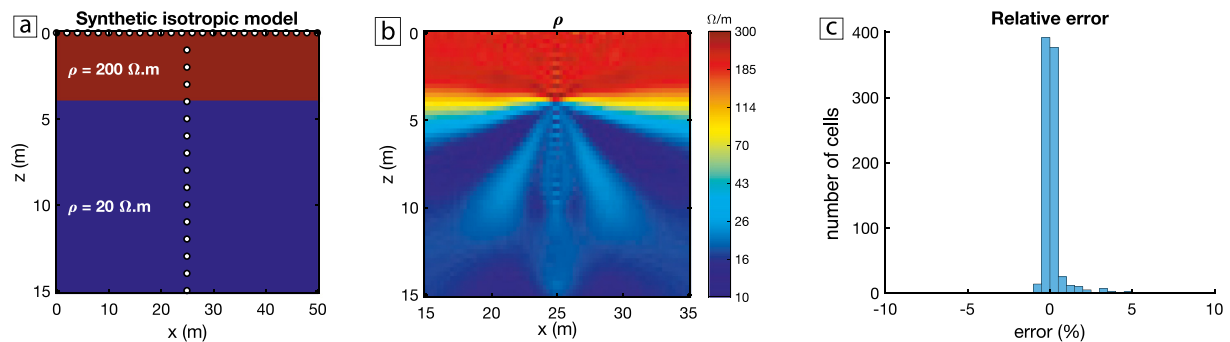


Fig. 6. Isotropic inverse modeling. Results from conventional isotropic inverse modeling from the same synthetic model as Fig. 5 ([a]). [b] Resistivity section. Note the logarithmic color scale. [c] Relative error between true synthetic and computed apparent resistivities.

The presented models have all been run on the same computing environment: MATLAB R2016b 64-bits run on a Intel(R) Core(TM) i9 9820X CPU (10 cores/20 threads, 3.3–4.10 GHz, 16.5 MB cache) with 128 GB of RAM. On this setup, it takes 120 s to perform the forward modeling shown in Fig. 2 and 67 s to perform the forward modeling shown in Fig. 3. Using the for-loop calculation, the anisotropic inverse modeling takes 380 s per iteration, while the conventional inverse modeling is faster with 80 s per iteration. Both AIM4RES and ERT2D can take advantage of parallel calculation using a parfor-loop for the sensitivity calculation. Using it on 10 cores, the anisotropic inverse modeling takes 165 s per iteration and the conventional inverse modeling takes 49 s per iteration. The difference in the iteration execution time is explained by two factors. First, the anisotropic inverse problem is a more underdetermined problem that shows a slower convergence and needs more iterations. Second, in the inverse modeling iteration, the sensitivity matrix size doubles between isotropic and anisotropic modeling, making the inverse calculation requiring more time. The sensitivity matrix is around 500 MB, showing that the CPU (clock rate

and cores number) has a greater influence on the calculation speed than the RAM amount.

5. Real case application

The proposed anisotropic algorithm was applied for a real case study at Saint-Lambert-de-Lauzon (Quebec, Canada). This site is an extensively characterized littoral aquifer system composed of finely interdigitated sandy and silty sediments that create important anisotropic groundwater flow (Paradis et al., 2014). The region is composed of horizontal to sub-horizontal layers, and we consider the angle of anisotropy θ to be zero. We then perform an ERT acquisition on an $9 \text{ m} \times 8 \text{ m}$ area, delimited by the surface and two wells in which borehole electrodes were used. A multi-array combination of 975 surface, in-hole, cross-hole and surface-borehole measurements has been acquired and inverted using our algorithm (Gernez et al., 2019). The inverted anisotropy section and distribution in Figs. 7.a and 7.b, respectively, show a strong degree of anisotropy varying by several orders

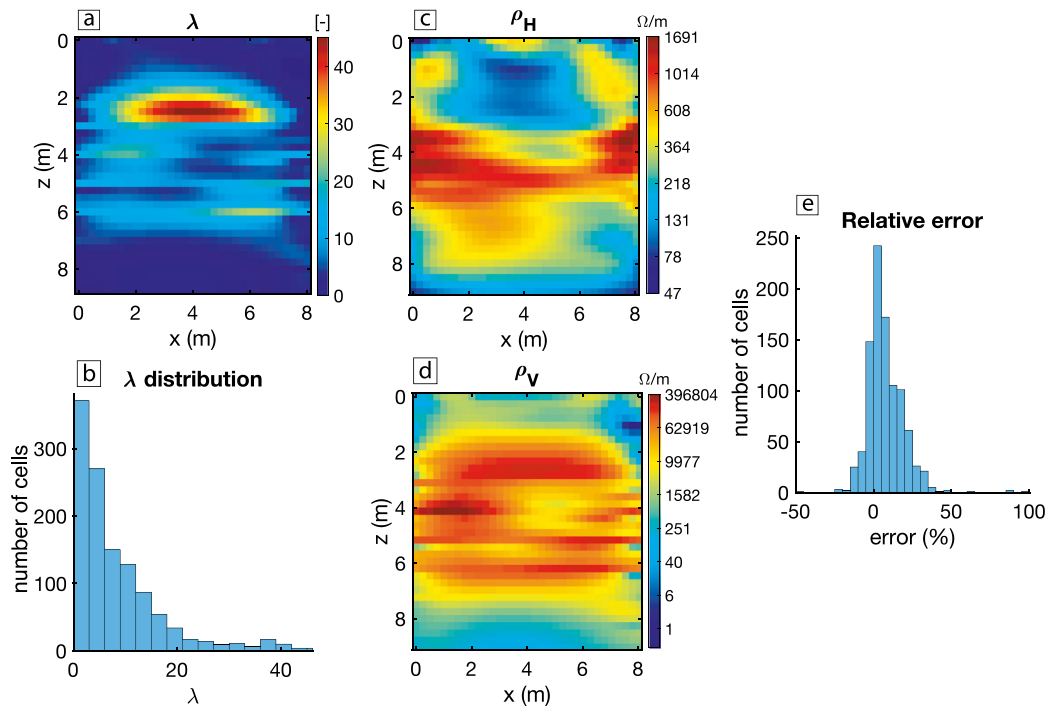


Fig. 7. Real case anisotropic study. Inverted results from apparent resistivity data acquired at Saint-Lambert-de-Lauzon, Quebec, Canada. [a] inverted anisotropy section. [b] anisotropy distribution. [c, d] respectively horizontal and vertical resistivity sections. Note the logarithmic color scale. [e] residual relative error.

of magnitude over short distances. Moreover, horizontal and vertical components of the resistivity tensor (Fig. 7.c and Fig. 7.d) show distinct patterns, highlighting the non-trivial relationship linking them. This was also observed by Paradis et al. (2016) with hydraulic conductivity for the same section using anisotropic inversion of hydraulic tomography data. Fig. 7.e shows the residual relative error between the observed and computed apparent resistivities. This error is higher for the real case study than for the synthetic study, for the obvious reason that the acquired data are not perfect as several noisy sources damage their quality. Nevertheless, 76% of the data shows a relative residual error lower than 15%, and 63% shows an error lower than 10%, and are acceptable considering a real case study.

6. Summary

Geological materials are inherently anisotropic due to the processes that lead to their deposition, and this anisotropy affects the geophysical techniques as Electrical Resistivity Tomography. This study presented AIM4RES, a fully functional finite-differences forward and inverse anisotropic modeling open source MATLAB library we developed to obtain more realistic estimates of the subsurface electrical resistivity. After AIM4RES implementation was detailed, we demonstrated its ability to properly infer the resistivity tensor through inversion, and hence to properly estimate the subsurface resistivity anisotropy. This was done with the help of a simple but realistic two layered synthetic example on which was used conventional borehole and surface ERT measurements. We showed that AIM4RES leads to accurate in situ characterization of the subsurface structures whether isotropic or moderately anisotropic. The isotropic inverted model from AIM4RES presented artifacts more pronounced than the isotropic inverted model from conventional modeling FD tools, due to the higher complexity of the anisotropic problem. However, these artifacts remain weak and the inverted model is consistent with the synthetic true model. The real case experiment revealed a strong degree of anisotropy varying by several orders of magnitude over short distances, suggesting that anisotropy may be a common property

of the subsurface, and demonstrating the ability of AIM4RES to handle anisotropy well. Gernez et al. (2019) have shown that anisotropy is well estimated even considering complex anisotropic environments, highlighting in this work the importance of the used arrays. It tends to prove that anisotropy should be considered in any electrical study when its presence is assumed, since considering it leads to more accurate electrical characterizations and better interpretations.

The source code, paper experiment scripts and general documentation are hosted on GitHub (<https://github.com/Simoger/AIM4RES>)

Computer code availability

Name of code: AIM4RES (Anisotropic Inverse Modeling for RESistivity)

AIM4RES source code was developed under MATLAB (version R2016b) by Simon GERNEZ with the precious help of Abderrezak BOUCHEDDA. The code was made available in 2019. It is a library working on any computational environment having MATLAB (Linux, OSX, Windows). The code is intended to be open source and freely available on GitHub: <https://github.com/Simoger/AIM4RES>. The repository contains the functions along with the script that allowed to produce the synthetic study figures. A description is also available to describe the used variables. Contacts: Simon.Gernez@ete.inrs.ca; Abderrezak.Bouchedda@ete.inrs.ca

Declaration of competing interest

The authors declare that they have no known competing financial interests or personal relationships that could have appeared to influence the work reported in this paper.

CRedit authorship contribution statement

Simon Gernez: Data curation, Methodology, Software, Writing - original draft, Writing - review and editing. **Abderrezak Bouchedda:**

Data curation, Methodology, Software, Supervision, Validation, Writing - review and editing. **Erwan Gloaguen**: Funding acquisition, Methodology, Resources, Supervision, Validation, Writing - review and editing. **Daniel Paradis**: Supervision, Writing - review and editing.

Acknowledgments

The authors want to acknowledge the NSERC discovery grant RGPIN-2018-06745 and the Canada Chair in Assimilation of Geological and Geophysical Data for Stochastic Geological Modelling of Pr. Gloaguen for funding this project. The authors would also like to thank the anonymous reviewers that helped to improve the initial manuscript. This is LMS contribution number 20190337.

Appendix A. Explicit forward finite differences

Considering the same development for the edges 2 to 8 as for the edge 1 (Eq. (13)), we obtain the following fully discretized finite differences equation:

$$\begin{aligned}
 & -\oint_L (\vec{\sigma} \cdot \nabla \tilde{\phi}) \cdot \mathbf{n} \, dl = \\
 & \left[\sigma_{i,j-1}^{xz} \frac{\tilde{\phi}_{i+1,j} - \tilde{\phi}_{i-1,j} + \tilde{\phi}_{i+1,j-1} - \tilde{\phi}_{i-1,j-1}}{2(\Delta x_{i-1} + \Delta x_i)} + \sigma_{i,j-1}^{zz} \frac{\tilde{\phi}_{i,j} - \tilde{\phi}_{i,j-1}}{\Delta z_{j-1}} \right] \frac{\Delta x_i}{2} \\
 & + \left[\sigma_{i,j-1}^{xx} \frac{\tilde{\phi}_{i,j} - \tilde{\phi}_{i+1,j}}{\Delta x_i} + \sigma_{i,j-1}^{xz} \frac{\tilde{\phi}_{i,j-1} - \tilde{\phi}_{i+1,j-1} + \tilde{\phi}_{i+1,j-1} - \tilde{\phi}_{i+1,j+1}}{2(\Delta z_{j-1} + \Delta z_j)} \right] \frac{\Delta z_{j-1}}{2} \\
 & + \left[\sigma_{i,j}^{xx} \frac{\tilde{\phi}_{i,j} - \tilde{\phi}_{i+1,j}}{\Delta x_i} + \sigma_{i,j}^{xz} \frac{\tilde{\phi}_{i,j-1} - \tilde{\phi}_{i+1,j-1} + \tilde{\phi}_{i+1,j-1} - \tilde{\phi}_{i+1,j+1}}{2(\Delta z_{j-1} + \Delta z_j)} \right] \frac{\Delta z_j}{2} \\
 & + \left[\sigma_{i,j}^{xz} \frac{\tilde{\phi}_{i-1,j} - \tilde{\phi}_{i+1,j} + \tilde{\phi}_{i-1,j+1} - \tilde{\phi}_{i+1,j+1}}{2(\Delta x_{i-1} + \Delta x_i)} + \sigma_{i,j}^{zz} \frac{\tilde{\phi}_{i,j} - \tilde{\phi}_{i,j+1}}{\Delta z_j} \right] \frac{\Delta x_i}{2} \quad (A.1) \\
 & + \left[\sigma_{i-1,j}^{xz} \frac{\tilde{\phi}_{i-1,j} - \tilde{\phi}_{i+1,j} + \tilde{\phi}_{i-1,j+1} - \tilde{\phi}_{i+1,j+1}}{2(\Delta x_{i-1} + \Delta x_i)} + \sigma_{i-1,j}^{zz} \frac{\tilde{\phi}_{i,j} - \tilde{\phi}_{i,j+1}}{\Delta z_j} \right] \frac{\Delta x_{i-1}}{2} \\
 & + \left[\sigma_{i-1,j}^{xx} \frac{\tilde{\phi}_{i,j} - \tilde{\phi}_{i-1,j}}{\Delta x_{i-1}} + \sigma_{i-1,j}^{xz} \frac{\tilde{\phi}_{i,j+1} - \tilde{\phi}_{i-1,j+1} + \tilde{\phi}_{i-1,j+1} - \tilde{\phi}_{i-1,j-1}}{2(\Delta z_{j-1} + \Delta z_j)} \right] \frac{\Delta z_j}{2} \\
 & + \left[\sigma_{i-1,j-1}^{xx} \frac{\tilde{\phi}_{i,j} - \tilde{\phi}_{i-1,j}}{\Delta x_{i-1}} + \sigma_{i-1,j-1}^{xz} \frac{\tilde{\phi}_{i,j+1} - \tilde{\phi}_{i-1,j+1} + \tilde{\phi}_{i-1,j+1} - \tilde{\phi}_{i-1,j-1}}{2(\Delta z_{j-1} + \Delta z_j)} \right] \frac{\Delta z_{j-1}}{2} \\
 & + \left[\sigma_{i-1,j-1}^{xz} \frac{\tilde{\phi}_{i+1,j} - \tilde{\phi}_{i-1,j} + \tilde{\phi}_{i+1,j-1} - \tilde{\phi}_{i-1,j-1}}{2(\Delta x_{i-1} + \Delta x_i)} + \sigma_{i-1,j-1}^{zz} \frac{\tilde{\phi}_{i,j} - \tilde{\phi}_{i,j-1}}{\Delta z_{j-1}} \right] \frac{\Delta x_{i-1}}{2}
 \end{aligned}$$

Let us now integrate the second term of Eq. (7) left part:

$$\begin{aligned}
 \iint_{\Delta A_{i,j}} k_{yy}^2 \sigma_{i,j} \tilde{\phi}_{i,j} \, dx_i dy_j &= k_{yy}^2 \left[\frac{\sigma_{i-1,j-1}^{yy} \Delta x_{i-1} \Delta z_{j-1}}{4} + \frac{\sigma_{i,j-1}^{yy} \Delta x_i \Delta z_{j-1}}{4} \right. \\
 & \quad \left. + \frac{\sigma_{i,j}^{yy} \Delta x_i \Delta z_j}{4} + \frac{\sigma_{i-1,j}^{yy} \Delta x_{i-1} \Delta z_j}{4} \right] \tilde{\phi}_{i,j} \\
 &= A \left(\sigma_{i,j}^{yy}, \Delta A_{i,j} \right) \tilde{\phi}_{i,j} \quad (A.2)
 \end{aligned}$$

We factorize Eqs. (A.1) and (A.2) under the form of Eq. (14):

$$\begin{aligned}
 C_{ij}^P \cdot \tilde{\phi}_{i,j} + C_{ij}^L \cdot \tilde{\phi}_{i-1,j} + C_{ij}^R \cdot \tilde{\phi}_{i+1,j} + C_{ij}^T \cdot \tilde{\phi}_{i,j-1} + C_{ij}^B \cdot \tilde{\phi}_{i,j+1} \\
 + C_{ij}^{TL} \cdot \tilde{\phi}_{i-1,j-1} \\
 + C_{ij}^{BL} \cdot \tilde{\phi}_{i-1,j+1} + C_{ij}^{TR} \cdot \tilde{\phi}_{i+1,j-1} + C_{ij}^{BR} \cdot \tilde{\phi}_{i+1,j+1} = \frac{I}{2} \delta(x_s) \delta(z_s)
 \end{aligned} \quad (14)$$

where

$$\begin{aligned}
 C_{ij}^L &= \frac{-\sigma_{i,j-1}^{xz} \Delta x_i + \sigma_{i,j}^{xz} \Delta x_i + \sigma_{i-1,j}^{xz} \Delta x_{i-1} - \sigma_{i-1,j-1}^{xz} \Delta x_{i-1}}{4(\Delta x_i + \Delta x_{i-1})} \\
 & - \frac{\Delta z_j \sigma_{i-1,j}^{xx} + \Delta z_{j-1} \sigma_{i-1,j-1}^{xx}}{2\Delta x_{i-1}} \quad (A.3a)
 \end{aligned}$$

is the coupling coefficient between nodes (i, j) and $(i - 1, j)$,

$$\begin{aligned}
 C_{ij}^R &= \frac{\sigma_{i,j-1}^{xz} \Delta x_i - \sigma_{i,j}^{xz} \Delta x_i - \sigma_{i-1,j}^{xz} \Delta x_{i-1} + \sigma_{i-1,j-1}^{xz} \Delta x_{i-1}}{4(\Delta x_i + \Delta x_{i-1})} \\
 & - \frac{\Delta z_j \sigma_{i,j}^{xx} + \Delta z_{j-1} \sigma_{i,j-1}^{xx}}{2\Delta x_i} \quad (A.3b)
 \end{aligned}$$

is the coupling coefficient between nodes (i, j) and $(i + 1, j)$,

$$\begin{aligned}
 C_{ij}^T &= \frac{\sigma_{i,j-1}^{xz} \Delta z_{j-1} + \sigma_{i,j}^{xz} \Delta z_j - \sigma_{i-1,j}^{xz} \Delta z_j - \sigma_{i-1,j-1}^{xz} \Delta z_{j-1}}{4(\Delta z_{j-1} + \Delta z_j)} \\
 & - \frac{\Delta x_i \sigma_{i,j-1}^{zz} + \Delta x_{i-1} \sigma_{i-1,j-1}^{zz}}{2\Delta z_{j-1}} \quad (A.3c)
 \end{aligned}$$

is the coupling coefficient between nodes (i, j) and $(i, j - 1)$,

$$\begin{aligned}
 C_{ij}^B &= \frac{-\sigma_{i,j-1}^{xz} \Delta z_{j-1} - \sigma_{i,j}^{xz} \Delta z_j + \sigma_{i-1,j}^{xz} \Delta z_j + \sigma_{i-1,j-1}^{xz} \Delta z_{j-1}}{4(\Delta z_{j-1} + \Delta z_j)} \\
 & - \frac{\Delta x_i \sigma_{i,j}^{zz} + \Delta x_{i-1} \sigma_{i-1,j}^{zz}}{2\Delta z_j} \quad (A.3d)
 \end{aligned}$$

is the coupling coefficient between nodes (i, j) and $(i, j + 1)$,

$$C_{ij}^{TL} = -\frac{\sigma_{i,j-1}^{xz} \Delta x_i + \sigma_{i-1,j-1}^{xz} \Delta x_{i-1}}{4(\Delta x_{i-1} + \Delta x_i)} - \frac{\sigma_{i-1,j}^{xz} \Delta z_j + \sigma_{i-1,j-1}^{xz} \Delta z_{j-1}}{4(\Delta z_{j-1} + \Delta z_j)} \quad (A.3e)$$

is the coupling coefficient between nodes (i, j) and $(i - 1, j - 1)$,

$$C_{ij}^{BL} = \frac{\sigma_{i,j}^{xz} \Delta x_i + \sigma_{i-1,j}^{xz} \Delta x_{i-1}}{4(\Delta x_{i-1} + \Delta x_i)} + \frac{\sigma_{i-1,j}^{xz} \Delta z_j + \sigma_{i-1,j-1}^{xz} \Delta z_{j-1}}{4(\Delta z_{j-1} + \Delta z_j)} \quad (A.3f)$$

is the coupling coefficient between nodes (i, j) and $(i - 1, j + 1)$,

$$C_{ij}^{TR} = \frac{\sigma_{i,j-1}^{xz} \Delta x_i + \sigma_{i-1,j-1}^{xz} \Delta x_{i-1}}{4(\Delta x_{i-1} + \Delta x_i)} + \frac{\sigma_{i,j}^{xz} \Delta z_j + \sigma_{i,j-1}^{xz} \Delta z_{j-1}}{4(\Delta z_{j-1} + \Delta z_j)} \quad (A.3g)$$

is the coupling coefficient between nodes (i, j) and $(i + 1, j - 1)$,

$$C_{ij}^{BR} = -\frac{\sigma_{i,j}^{xz} \Delta x_i + \sigma_{i-1,j}^{xz} \Delta x_{i-1}}{4(\Delta x_{i-1} + \Delta x_i)} - \frac{\sigma_{i,j-1}^{xz} \Delta z_j + \sigma_{i,j-1}^{xz} \Delta z_{j-1}}{4(\Delta z_{j-1} + \Delta z_j)} \quad (A.3h)$$

is the coupling coefficient between nodes (i, j) and $(i + 1, j + 1)$, and finally

$$\begin{aligned}
 C_{ij}^P &= - \left[C_{ij}^L + C_{ij}^R + C_{ij}^T + C_{ij}^B + C_{ij}^{TL} + C_{ij}^{BL} + C_{ij}^{TR} + C_{ij}^{BR} - A \left(\sigma_{i,j}^{yy}, \Delta A_{i,j} \right) \right] \quad (A.3i)
 \end{aligned}$$

These equations are implemented in the function `matrix_coeff_anis.m`.

Appendix B. Explicit inverse finite differences

The sensitivity is obtained discretizing Eq. (23).

$$\begin{aligned}
 \frac{\partial \tilde{\phi}}{\partial p} &= - \left\{ \frac{\partial \sigma_{xx}}{\partial p} \frac{\partial \tilde{\phi}}{\partial x} \frac{\partial G}{\partial x} + \frac{\partial \sigma_{zz}}{\partial p} \frac{\partial \tilde{\phi}}{\partial z} \frac{\partial G}{\partial z} + \frac{\partial \sigma_{xz}}{\partial p} \left(\frac{\partial \tilde{\phi}}{\partial x} \frac{\partial G}{\partial z} + \frac{\partial \tilde{\phi}}{\partial z} \frac{\partial G}{\partial x} \right) + k_{yy}^2 \frac{\partial \sigma_{yy}}{\partial p} \tilde{\phi} G \right\} \quad (B.1)
 \end{aligned}$$

We explicit here the needed gradient products, as they are implemented in `gradient_product_anis.m`.

The horizontal gradient product is:

$$\begin{aligned}
 \frac{\partial \tilde{\phi}}{\partial x} \frac{\partial G}{\partial x} &= \left[(\tilde{\phi}_{i+1,j} - \tilde{\phi}_{i,j}) (G_{i+1,j} - G_{i,j}) + (\tilde{\phi}_{i+1,j+1} - \tilde{\phi}_{i,j+1}) (G_{i+1,j+1} - G_{i,j+1}) \right]
 \end{aligned}$$

$$\begin{aligned}
& + \frac{\left(\tilde{\phi}_{i+1,j} + \tilde{\phi}_{i+1,j+1} - \tilde{\phi}_{i-1,j} - \tilde{\phi}_{i-1,j+1} \right)}{4} \frac{\left(G_{i+1,j} + G_{i+1,j+1} - G_{i-1,j} - G_{i-1,j+1} \right)}{4} \\
& + \frac{\left(\tilde{\phi}_{i+2,j} + \tilde{\phi}_{i+2,j+1} - \tilde{\phi}_{i,j} - \tilde{\phi}_{i,j+1} \right)}{4} \frac{\left(G_{i+2,j} + G_{i+2,j+1} - G_{i,j} - G_{i,j+1} \right)}{4} \Big] \Delta x_i \Delta z_j
\end{aligned} \tag{B.2}$$

The vertical gradient product is:

$$\begin{aligned}
& \frac{\partial \tilde{\phi}}{\partial z} \frac{\partial G}{\partial z} \\
& = \left[\left(\tilde{\phi}_{i,j+1} - \tilde{\phi}_{i,j} \right) \left(G_{i,j+1} - G_{i,j} \right) + \left(\tilde{\phi}_{i+1,j+1} - \tilde{\phi}_{i+1,j} \right) \left(G_{i+1,j+1} - G_{i+1,j} \right) \right. \\
& + \frac{\left(\tilde{\phi}_{i+1,j} + \tilde{\phi}_{i+1,j+1} - \tilde{\phi}_{i-1,j} - \tilde{\phi}_{i-1,j+1} \right)}{4} \frac{\left(G_{i+1,j} + G_{i+1,j+1} - G_{i-1,j} - G_{i-1,j+1} \right)}{4} \\
& \left. + \frac{\left(\tilde{\phi}_{i,j+2} + \tilde{\phi}_{i+1,j+2} - \tilde{\phi}_{i,j} - \tilde{\phi}_{i,j+1} \right)}{4} \frac{\left(G_{i,j+2} + G_{i+1,j+2} - G_{i,j} - G_{i+1,j} \right)}{4} \right] \Delta x_i \Delta z_j
\end{aligned} \tag{B.3}$$

The sum of the cross gradient product is:

$$\begin{aligned}
& \frac{\partial \tilde{\phi}}{\partial x} \frac{\partial G}{\partial z} + \frac{\partial \tilde{\phi}}{\partial z} \frac{\partial G}{\partial x} = \\
& \left(\tilde{\phi}_{i+1,j} - \tilde{\phi}_{i,j} \right) \left(G_{i,j+1} + G_{i+1,j+1} - G_{i,j-1} - G_{i+1,j-1} \right) \\
& + \left(\tilde{\phi}_{i+1,j+1} - \tilde{\phi}_{i,j+1} \right) \left(G_{i,j+2} + G_{i+1,j+2} - G_{i,j} - G_{i+1,j} \right) \\
& + \left(\tilde{\phi}_{i,j+1} - \tilde{\phi}_{i,j} \right) \left(G_{i+1,j} + G_{i+1,j+1} - G_{i-1,j} - G_{i-1,j+1} \right) \\
& + \left(\tilde{\phi}_{i+1,j+1} - \tilde{\phi}_{i+1,j} \right) \left(G_{i+2,j+1} + G_{i+2,j} - G_{i,j+1} - G_{i,j} \right) \\
& + \left(G_{i+1,j} - G_{i,j} \right) \left(\tilde{\phi}_{i,j+1} + \tilde{\phi}_{i+1,j+1} - \tilde{\phi}_{i-1,j} - \tilde{\phi}_{i-1,j+1} \right) \\
& + \left(G_{i+1,j+1} - G_{i,j+1} \right) \left(\tilde{\phi}_{i,j+2} + \tilde{\phi}_{i+1,j+2} - \tilde{\phi}_{i,j} - \tilde{\phi}_{i,j+1} \right) \\
& + \left(G_{i,j+1} - G_{i,j} \right) \left(\tilde{\phi}_{i+1,j} + \tilde{\phi}_{i+1,j+1} - \tilde{\phi}_{i-1,j} - \tilde{\phi}_{i-1,j+1} \right) \\
& + \left(G_{i+1,j+1} - G_{i+1,j} \right) \left(\tilde{\phi}_{i+2,j+1} + \tilde{\phi}_{i+2,j} - \tilde{\phi}_{i,j+1} - \tilde{\phi}_{i,j} \right)
\end{aligned} \tag{B.4}$$

The details of $\frac{\partial \sigma_i}{\partial p}$ are found in Greenhalgh et al. (2009) and are implemented in `calcul_u_s_anis.m`.

References

- Al-Hazaimay, S., Huisman, J.A., Zimmermann, E., Vereecken, H., 2016. Using electrical anisotropy for structural characterization of sediments: an experimental validation study. *Near Surf. Geophys.* 14 (4), 357–369.
- Amatyakul, P., Vachiratanchai, C., Siripunvaraporn, W., 2017. WSJointInv2D-MT-DCR: An efficient joint two-dimensional magnetotelluric and direct current resistivity inversion. *Comput. Geosci.* 102, 100–108.
- Asten, M., 1974. The influence of electrical anisotropy on mise a la masse surveys. *Geophys. Prospect.* 22 (2), 238–245.
- Bauman, P., 2005. 2-D resistivity surveying for hydrocarbons—a primer. *CSEG Recorder* 30 (4), 25–33.
- Binley, A., Kemna, A., 2005. DC resistivity and induced polarization methods. In: *Hydrogeophysics*. Springer, pp. 129–156.
- Bouchedda, A., 2010. Inversion conjointe des données électriques et de radar en forage. *École Polytechnique de Montréal*.
- Cassiani, G., Bruno, V., Villa, A., Fusi, N., Binley, A.M., 2006. A saline trace test monitored via time-lapse surface electrical resistivity tomography. *J. Appl. Geophys.* 59 (3), 244–259. <http://dx.doi.org/10.1016/j.jappgeo.2005.10.007>, URL <http://www.sciencedirect.com/science/article/pii/S0926985105000911>.
- Chambers, J.E., Kuras, O., Meldrum, P.I., Ogilvy, R.D., Hollands, J., 2006. Electrical resistivity tomography applied to geologic, hydrogeologic, and engineering investigations at a former waste-disposal site. *Geophysics* 71 (6), B231–B239.
- Corwin, D.L., Lesch, S.M., 2003. Application of soil electrical conductivity to precision agriculture. *Agron. J.* 95 (3), 455. <http://dx.doi.org/10.2134/agronj2003.0455>.

- Dey, A., Morrison, H., 1979. Resistivity modelling for arbitrarily shaped two-dimensional structures. *Geophys. Prospect.* 27 (1), 106–136.
- van Es, B., Koren, B., de Blank, H.J., 2014. Finite-difference schemes for anisotropic diffusion. *J. Comput. Phys.* 272, 526–549.
- de Franco, R., Biella, G., Tosi, L., Lozej, A., Chiozzotto, B., Giada, M., Rizzetto, F., Claude, C., Mayer, A., Bassan, V., Gasparetto-Stori, G., 2009. Monitoring the saltwater intrusion by time lapse electrical resistivity tomography: The chioggia test site (Venice Lagoon, Italy). *J. Appl. Geophys.* 69 (3), 117–130. <http://dx.doi.org/10.1016/j.jappgeo.2009.08.004>, URL <http://www.sciencedirect.com/science/article/pii/S0926985109001062>.
- Gernez, S., Bouchedda, A., Gloaguen, E., Paradis, D., 2019. Comparison between hydraulic conductivity anisotropy and electrical resistivity anisotropy from tomography inverse modeling. *Front. Environ. Sci.*
- Greenhalgh, S., Wiese, T., Marescot, L., 2010. Comparison of DC sensitivity patterns for anisotropic and isotropic media. *J. Appl. Geophys.* 70 (2), 103–112.
- Greenhalgh, S.A., Zhou, B., Greenhalgh, M., Marescot, L., Wiese, T., 2009. Explicit expressions for the Fréchet derivatives in 3D anisotropic resistivity inversion. *Geophysics* 74 (3), F31–F43.
- Günther, T., Rücker, C., 2009. Advanced inversion strategies using a new geophysical inversion and modelling library. In: *Near Surface 2009 - 15th EAGE European Meeting of Environmental and Engineering Geophysics*. EAGE Publications BV, <http://dx.doi.org/10.3997/2214-4609.20147039>.
- Herwanger, J.V., Pain, C.C., Binley, A., De Oliveira, C.R.E., Worthington, M.H., 2004. Anisotropic resistivity tomography. *Geophys. J. Int.* 158 (2), 409–425. <http://dx.doi.org/10.1111/j.1365-246X.2004.02314.x>, URL <https://onlinelibrary.wiley.com/doi/abs/10.1111/j.1365-246X.2004.02314.x>.
- Hubbard, S.S., Rubin, Y., 2005. Introduction to hydrogeophysics. In: *Hydrogeophysics*. Springer, pp. 3–21.
- Ingeman-Nielsen, T., Baumgartner, F., 2006. CR1Dmod: A matlab program to model 1d complex resistivity effects in electrical and electromagnetic surveys. *Comput. Geosci.* 32 (9), 1411–1419.
- Ismail, A., Anderson, N.L., Rogers, J., 2005. Hydrogeophysical investigation at luxor, southern Egypt. *J. Environ. Eng. Geophys.* 10 (1), 35–49.
- Johnson, T.C., Hammond, G.E., Chen, X., 2017. PFLOTTRAN-E4D: A parallel open source PFLOTTRAN module for simulating time-lapse electrical resistivity data. *Comput. Geosci.* 99, 72–80.
- Keller, G.V., Frischknecht, F.C., 1966. *Electrical Methods in Geophysical Prospecting*. Pergamon.
- Kemna, A., Vanderborght, J., Kulesha, B., Vereecken, H., 2002. Imaging and characterisation of subsurface solute transport using electrical resistivity tomography (ERT) and equivalent transport models. *J. Hydrol.* 267 (3), 125–146. [http://dx.doi.org/10.1016/S0022-1694\(02\)00145-2](http://dx.doi.org/10.1016/S0022-1694(02)00145-2), URL <http://www.sciencedirect.com/science/article/pii/S0022169402001452>.
- LaBrecque, D.J., Miletto, M., Daily, W., Ramirez, A., Owen, E., 1996. The effects of noise on Occam's inversion of resistivity tomography data. *Geophysics* 61 (2), 538–548. <http://dx.doi.org/10.1190/1.1443980>.
- LaBrecque, D.J., Yang, X., 2001. Difference inversion of ERT data: A fast inversion method for 3-D in situ monitoring. *J. Environ. Eng. Geophys.* 6 (2), 83–89.
- Li, Y., Oldenburg, D.W., 1996. Joint inversion of surface and three-component borehole magnetic data. In: *SEG Technical Program Expanded Abstracts 1996*. Society of Exploration Geophysicists, pp. 1142–1145.
- Li, P., Uren, N.F., 1998. Analytical solution for the electric potential due to a point source in an arbitrarily anisotropic half-space. *J. Engrg. Math.* 33 (2), 129–140.
- Loke, M., Dahlin, T., Rucker, D.F., 2013. Smoothness-constrained time-lapse inversion of data from 3D resistivity surveys. *Near Surf. Geophys.* 12 (1), 5–24. <http://dx.doi.org/10.3997/1873-0604.2013025>.
- Maillet, R., 1947. The fundamental equations of electrical prospecting. *Geophysics* 12 (4), 529–556. <http://dx.doi.org/10.1190/1.1437342>.
- Menke, W., 1989. *Geophysical Data Analysis: Discrete Inverse Theory*. p. 289.
- Neyamadpour, A., Taib, S., Abdullah, W.W., 2009. Using artificial neural networks to invert 2d DC resistivity imaging data for high resistivity contrast regions: A MATLAB application. *Comput. Geosci.* 35 (11), 2268–2274.
- Pain, C.C., Herwanger, J.V., Saunders, J.H., Worthington, M.H., de Oliveira, C.R., 2003. Anisotropic resistivity inversion. *Inverse Problems* 19 (5), 1081.
- Papadopoulos, N.G., Yi, M.-J., Kim, J.-H., Tsourlos, P., Tsokas, G.N., 2010. Geophysical investigation of tumuli by means of surface 3D electrical resistivity tomography. *J. Appl. Geophys.* 70 (3), 192–205. <http://dx.doi.org/10.1016/j.jappgeo.2009.12.001>, URL <http://www.sciencedirect.com/science/article/pii/S0926985109001554>.
- Paradis, D., Gloaguen, E., Lefebvre, R., Giroux, B., 2016. A field proof-of-concept of tomographic slug tests in an anisotropic littoral aquifer. *J. Hydrol.*
- Paradis, D., Tremblay, L., Lefebvre, R., Gloaguen, E., Rivera, A., Parent, M., Ballard, J.-M., Michaud, Y., Brunet, P., 2014. Field characterization and data integration to define the hydraulic heterogeneity of a shallow granular aquifer at a sub-watershed scale. *Environ. Earth Sci.* 72 (5), 1325–1348.
- Pidlisecky, A., Knight, R., 2008. FW2_5D: A MATLAB 2.5-D electrical resistivity modeling code. *Comput. Geosci.* 34 (12), 1645–1654.
- Pidlisecky, A., Knight, R., Haber, E., 2006. Cone-based electrical resistivity tomography. *Geophysics* 71 (4), G157–G167. <http://dx.doi.org/10.1190/1.2213205>.
- Polydorides, N., Lionheart, W.R., 2002. A matlab toolkit for three-dimensional electrical impedance tomography: a contribution to the electrical impedance and diffuse optical reconstruction software project. *Meas. Sci. Technol.* 13 (12), 1871.

- Santarato, G., Ranieri, G., Occhi, M., Morelli, G., Fischanger, F., Gualerzi, D., 2011. Three-dimensional electrical resistivity tomography to control the injection of expanding resins for the treatment and stabilization of foundation soils. *Eng. Geol.* 119 (1–2), 18–30. <http://dx.doi.org/10.1016/j.enggeo.2011.01.009>.
- Singh, K., B.S.singh, K., Lokhande, R., Prakash, A., 2004. Multielectrode resistivity imaging technique for the study of coal seam. *J. Sci. Ind. Res.* 63.
- Singh, U.K., Tiwari, R., Singh, S., 2005. One-dimensional inversion of geo-electrical resistivity sounding data using artificial neural networks—a case study. *Comput. Geosci.* 31 (1), 99–108.
- Telford, W.M., Geldart, L.P., Sheriff, R.E., 1990. *Applied Geophysics*, vol. 1, Cambridge University Press.
- Tikhonov, A.N., Arsenin, V.Y., 1977. *Solutions of Ill-Posed Problems*. V. H. Winston & Sons, Washington, D.C., John Wiley & Sons, New York.
- Xu, B., Noel, M., 1991. Archaeological investigation by electrical resistivity tomography: a preliminary study. *Geophys. J. Int.* 107 (1), 95–102. <http://dx.doi.org/10.1111/j.1365-246X.1991.tb01159.x>, arXiv:<http://oup.prod.sis.lan/gji/article-pdf/107/1/95/1840162/107-1-95.pdf>.
- Zhou, B., Greenhalgh, M., Greenhalgh, S.A., 2009. 2.5-D/3-D resistivity modelling in anisotropic media using Gaussian quadrature grids. *Geophys. J. Int.* 176 (1), 63–80.